AMERICAN SCIENTIFIC PUBLISHERS

*Reviews in Nanoscience and Nanotechnology*
Vol. 3, pp. 193–209, 2014
(www.aspbs.com/rnn)

# Capillary-Type Microfluidic Sensors Based on Optical Whispering Gallery Mode Resonances

**A. Meldrum* and F. Marsiglio**

*Department of Physics, University of Alberta, Edmonton, AB, T6G2E1, Canada*

Microfluidic capillary-type sensors could potentially find applications in a range of medical and environmental diagnostic technologies. Refractive-index sensors-as well as biosensors-based on the whispering gallery mode resonances of a thin-walled capillary offer several modes of operation and the capacity to detect a wide range of analytes through standard silica surface functionalization methods. This article reviews the basic optical physics associated with the resonances and how they respond to changes in the local refractive index. The sensitivity and detection limits of these devices are explored, and at least one old assumption concerning the inverse relationship between the quality factor of the resonance and the detection limit is shown to be valid only under a restricted set of circumstances. Problems and pitfalls associated with whispering-gallery-mode capillary sensors are examined, as well as the experimental methods needed for analysis. Finally, relevant capillary sensor examples from the literature are summarized.

**KEYWORDS:** Liquid Core Optical Ring Resonator, Fluorescent Core Microcapillary, Capillary, Sensor, Microfluidic, Whispering Gallery Modes.



## CONTENTS



## 1. INTRODUCTION

Capillaries have been widely investigated for their many chemical and biochemical sensor-related applications.[1–3] A variety of sensing transduction techniques can be employed and have been reviewed,[4,5] including capillary electrophoresis,[6–10] fiber-optic methods that couple light into and out of a capillary[11] (e.g., Bragg gratings), and simple optical refractive index sensors.[12,13] Microfluidic operation can be especially interesting for the development of small, parallelized devices or for situations in which the sample volume is small.[14–16]

Thin-walled glass capillaries represent one promising avenue toward the development of microfluidic optical sensors. The outer wall traps light by total internal reflection as it circulates around the capillary circumference, while fluids can be pumped into the channel region. The cylindrical electromagnetic resonances that form the basis of the transduction mechanism are called the whispering gallery modes (WGMs).

WGMs have been the subject of several recent reviews that have focused mainly on the properties of optical microspheres.[17–19] Optical resonances in microdisks[20] and pillars[21] have also been widely investigated and reviewed, partly due to the ability to control the spontaneous emission rate for atoms or quantum dots placed in the cavity.[22–26] The cylindrical WGMs have also been reviewed,[27,28] although mostly without a sensor[29] focus. The intent of this work is to overview the work so far on capillary WGM-type sensor structures, and to outline the basic physics and experimental issues that would be helpful for researchers wishing to enter the field.

*Author to whom correspondence should be addressed.
Email: ameldrum@ualberta.ca
Received: 21 December 2013
Accepted: 28 June 2014

## 2. HISTORICAL BACKGROUND

The term "whispering gallery" seems to have originated to describe the peculiar acoustic effects that were reported in domed buildings such as St. Paul's cathedral in London[30] and the Gol Gumbaz Mausoleum in northern India.[31] In these circular domed structures, a whisper at one side is clearly audible at the other side of the dome, but it cannot be heard near the center. Lord Rayleigh's 1910 paper titled "The problem of the whispering gallery"[30] specifically focused on what he called an acoustic "clinging effect." Essentially, the "sonorous vibrations" produced near one wall of the cathedral appeared spatially limited to a tiny fraction of the radius very near the cathedral wall at the other side (as measured by the flicker of a candle flame!). Lord Rayleigh's paper reported that the Bessel function $J_l(z)$, which was the known solution for a circular resonance with fixed boundaries, has interesting properties if $l$ is large. In such cases, he showed that the resonant vibrations must indeed "cling" very near to the outer radius of the resonator and are nearly zero inside, exactly as observed.

Gustav Mie had, just a few years earlier, developed the theory for the scattering of light by small aerosol droplets.[32] These structures were known to have electromagnetic resonances that were similar in many respects to Lord Rayleigh's whispering gallery modes, and the name eventually referred to both the acoustic and optical resonances. Part of Mie's work was based on earlier light scattering studies by Thomson,[33] Alfred Clebsch,[34] Ludwig Lorenz,[35,36] and Peter Debye.[37] A complete history of Mie's electromagnetic scattering theory was assembled by Horvath[38] and by Wriedt,[39] and these are excellent sources for a more complete history of the WGMs. Essentially, while the basic properties of optical WGMs were understood in the early part of the 20th century, the mathematics describing the Bessel functions needed in the Mie theory were for the most part too complicated to be fully treated until the advent of computers. Much more recent efforts gave complete, modern descriptions of the spherical WGMs.[40,41]

Cylindrical structures have a set of resonances that are similar to the spherical ones, the main difference being that there is no polar component to the field, which can be assumed to propagate in a 2-dimensional cylindrical cross section similar to Rayleigh's acoustic modes (the effect of waves with some component of their wavevector along the capillary axis will also be discussed, however). The equations used to model the resonances are mainly the same as for the spherical case, with the main differences being the use of cylindrical rather than spherical Bessel functions and the lack of a "polar" direction (i.e., one need not consider the Legendre harmonics) in the field solutions.

Thus, only a few parameters are needed to completely describe the capillary resonances: the number of intensity maxima in the radial direction ($n$), the number of wavelengths that "fit" around the cylinder for a given resonance ($l$), and the quality ($Q$) factor that describes how well the mode is able to trap radiation. Three such resonances are illustrated in Figure 1, showing different values of $n$. The polarization can be either transverse electric (TE) or transverse magnetic (TM). Unfortunately, there is no consensus as to the definition of the polarization



**A. Meldrum** obtained his Ph.D. in 1997 from the University of New Mexico, where he studied radiation-solid interactions in materials for nuclear waste disposal. He went on to a postdoctoral fellowship at Oak Ridge National Laboratory, working on the microstructure and properties of semiconductor and magnetic nanocrystals. Dr. Meldrum joined the University of Alberta as Assistant Professor in physics in September 1999. Currently he focuses on optical cavities, optical sensors, fluorescence imaging and spectroscopy, and the basic physics of cavity-quantum-dot interactions. He additionally works on new ways to bring research into the classrooms and to provide undergrads a greater exposure to physics research. Now a full professor and Vargo Teaching chair, he has more than 130 refereed publications in physics, materials science, optics, and earth science journals.

**F. Marsiglio** graduated with a B.A.Sc. from the Engineering Science program at the University of Toronto in 1983, then went on to do graduate work in physics at McMaster University, where he received both a Masters and Ph.D. (1988). Subsequently he held an NSERC postdoctoral fellowship at the University of California, San Diego. In 1990 he joined AECL Research at Chalk River Laboratories. During this time his work has focused on the theory of superconductivity, particularly as applied to the so-called high temperature superconductors. In 1997 he became an associate professor in the Department of Physics at the University of Alberta, and a full professor in 2001. Coincidentally he became the Director of the Theoretical Physics Institute and kept this position until 2008. In 2013 he became Associate Chair of Research in the department. He was a member of the Quantum Materials Program in the Canadian Institute for Advanced Research. His research covers superconductivity, polarons, non-equilibrium magnetism, and resonances in optical cavities.

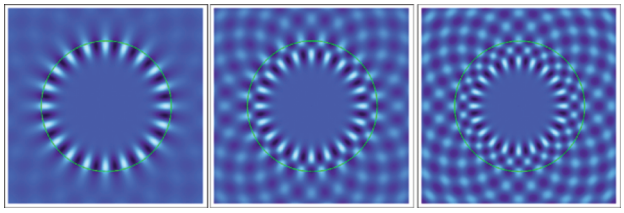

**Fig. 1.** Electric field amplitude for the first three transverse electric radial mode orders $n = 1, 2, 3$ of a disk. All three resonances have the same angular mode order $l = 20$ and are TE polarized. The disk boundary is denoted by the thin green line.

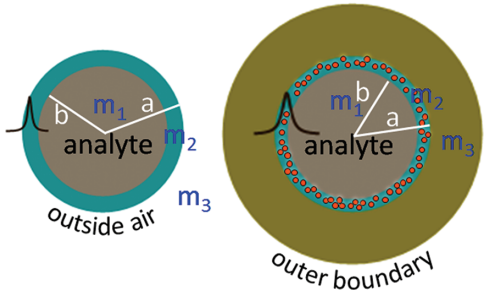


**Fig. 2.** Sketch of the LCORR (left) and FCM (right) structures. In both devices, $m_1$ is the analyte refractive index and $m_3$ is the outside index (air in the LCORR case, the glass capillary wall in the FCM). The confining layer has index $m_2$; it is comprised of the thinned capillary wall (in the LCORR) or a thin fluorescent layer (for the FCM), which can typically be made of quantum dots (the dotted layer in the right-hand diagram). The electric field profile of a resonance is sketched superimposed onto the diagram (the black "wave"). In the case of the FCM, the outer capillary boundary is mostly irrelevant, since it is typically located very far from the fluorescent film and channel regions.

directions for capillaries. We prefer to define the polarization with respect to the WGM propagation plane; thus TE resonances have the electric field parallel to the capillary axis, whereas TM modes have the magnetic field parallel to the axis.

The two main types of device structures are the liquid–core optical ring resonator (LCORR) and the fluorescent core microcapillary (FCM). Both are three-layer cylindrical cavity structures (Fig. 2). In the case of the liquid–core optical ring resonator, the light-confining region (index $m_2$) is the thinned wall of a glass capillary and the outer region ($m_3$) is air. In the case of the FCM, the confining region is a high-index fluorescent film and the outer region is the thick wall of the capillary. In order to confine radiation into the cylindrical resonances of either structure, $m_2$ must be larger than $m_3$ (unless layer 2 is very thin, in which case $m_1$ should also be greater than $m_3$). The analyte ($m_1$) is in the channel region for both structures. As illustrated in Figure 2, the FCM is a larger and more physically robust device.

## 3. CYLINDRICAL WGMs: BASIC CONCEPTS

Here we are interested in solving the electric field distribution for the WGM resonances of a layered cylinder. The purpose of this section is not a rigorous re-derivation of the cylindrical resonances, which can be found in different formats from several sources (e.g., Refs. [42–44]), but is instead aimed toward a practical and more easily understandable method to solve the electric field resonances, which that can be readily implemented. The solutions permit a straightforward calculation of the mode wavelength, $Q$ factor, and the refractometric and thermal sensitivity for LCORRs (which are synonymous with opto-fluidic ring resonators, or "OFRRs"), fluorescent core microcapillaries (FCMs), or other layered cylindrical structures such as coated optical fibers[45] or microdisks. We will examine a 3-layer system since the two main types of experimental realization are effectively comprised of only three layers: a channel analyte, a confining region responsible for the development of the WGMs, and an outside region. However, the theory can be extended to four or more layers relatively easily.

We review the TE polarization first, since it is simpler. The E-field is by definition parallel to the capillary axis. The radial and azimuthal components of the field are zero, and the axial part is usually solved by separation of variables:

$$E_z(r, \phi) = E_z(r) \exp(\pm il\phi) \tag{1}$$

Here, $r$ and $\phi$ are the cylinder's radial direction and azimuthal angle, respectively, and the axial direction will be $z$. The electric field has been separated into a radial part $E_z(r)$ and an azimuthal part, $e^{il\phi}$; the latter implies that the field will return to the starting point in phase after making $l$ oscillations (note that use of integer $m$ rather than $l$ would be more consistent with respect to a derivation of the spherical resonances, but here $m$ is reserved for the refractive index and $n$ for the radial mode number). Other periodic functions could be used in Eq. (1), but $e^{il\phi}$ represents a simple solution for an azimuthally uniform cylindrical structure. The time dependence of the field will be described later.

According to Maxwell's equations the TE resonances of a dielectric cylinder must satisfy:

$$\nabla^2 E_z(r, \phi) + \frac{\partial}{\partial z}\left(E_z(r, \phi)\frac{1}{\varepsilon}\frac{\partial \varepsilon(r)}{\partial z}\right) + k_0^2 m^2 E_z(r, \phi) = 0 \tag{2}$$

where $\varepsilon$ is the electric permittivity of the material in which the field is propagating, $k_0$ is the vacuum wavevector and $m$ is the refractive index, and $E_z$ is the electric field polarized along the capillary axis. The second term is zero because the index of refraction is taken to be constant in the $z$-direction. The Laplacian operator in cylindrical coordinates is

$$\nabla^2 E_z(r, \phi) = \frac{\partial^2 E_z(r, \phi)}{\partial z^2} + \frac{1}{r^2}\frac{\partial^2 E_z(r, \phi)}{\partial \phi^2} + \frac{1}{r}\frac{\partial}{\partial r} \times \left(r\frac{\partial E_z(r, \phi)}{\partial r}\right) \tag{3}$$

The first term on the right-hand side is also zero since we assume no axial ($z$) variation of the electric field in the cylinder, which simplifies the analysis. The second term is

$$\frac{1}{r^2}\frac{\partial^2 E_z(r,\phi)}{\partial\phi^2} = \frac{1}{r^2}\frac{\partial^2 (E_z(r,\phi)e^{il\phi})}{\partial\phi^2} = -\frac{l^2}{r^2}E_z(r) \quad (4)$$

and the third term can be written

$$\frac{1}{r}\frac{\partial}{\partial r}\frac{r\cdot\partial E_z(r,\phi)}{\partial r} = \frac{\partial^2 E_z(r,\phi)}{\partial r^2} + \frac{1}{r}\frac{\partial E_z(r,\phi)}{\partial r} \quad (5)$$

Combining Eqs. (2)–(5), multiplying both sides by $r^2$, and separating variables according to Eq. (1) gives:

$$e^{\pm il\phi}\left[r^2\frac{d^2E_z(r)}{dr^2} + r\frac{dE_z(r)}{dr} + (k^2r^2m^2 - l^2)E_z(r)\right] = 0 \quad (6)$$

The radial part of Eq. (6) can be rewritten in the standard form using $R = mkr$ and $dR = mk\cdot dr$:

$$R^2\frac{d^2E_z(R)}{dR^2} + R\frac{dE_z(R)}{dR} + (R^2 - l^2)E_z(R) = 0 \quad (7)$$

This is the Bessel differential equation with solutions for $E_z(R)$ given by linear combinations of $J_l(R)$ and $Y_l(R)$; i.e., cylindrical Bessel functions of the first and second kind, of order $l$. The cylindrical Hankel functions $H_l^{(1)}(R) = J_l(R) + iY_l(R)$ and $H_l^{(2)}(R) = J_l(R) - iY_l(R)$ are also solutions of Eq. (7) and will be important for the radiating fields, as described further below.

For the electric field resonance in a layered cylinder we need to solve Eq. (7) when there are piecewise discontinuities in the refractive index such that:

$$m(r) = \left\{\begin{array}{ll} m_1, & r \le b \\ m_2, & b < r \le a \\ m_3, & r > a \end{array}\right\} \quad (8)$$

Here, $a$ is the radius of the outer boundary of the layered cylinder, and $b = a - t$ is the radius of the inner one, where $t$ is the confining layer thickness. For an FCM, $t$ will represent the thickness of the fluorescent layer, and for an LCORR it is the thickness of the capillary wall.

The solution for $E_z(R)$ in each of the three regions depends on the boundary conditions. For the inner layer (layer 1), the requirement is that the field not be infinite at the origin so the Bessel function of the first kind is the only solution; that is, $E_z(R) = A_lJ_l(R)$. In the outermost layer, the waves should be traveling outwards. For large argument $mkr$, an asymptotic expansion of the Hankel function yields

$$H_l^{(1)}(mkr) = \sqrt{\frac{2}{\pi mkr}}e^{i(mkr - l\pi/2 - \pi/4)} \quad (9)$$

which represents an "outgoing" wave in the time-dependent wave equation. This implies that the field in the outermost layer is described by $E_z(R) = D_lH_l^{(1)}(R) = D_l[J_l(R) + iY_l(R)]$, where $D_l$ is another constant.

In the middle layer (layer 2), we have both incoming and outgoing waves. The incoming waves are described by $H_l^{(2)}(R) = J_l(R) - iY_l(R)$, which leads to the same expansion as shown in Eq. (9), except with the opposite sign in the exponential term. Thus, the field within layer 2 can be described as $E_z(R) = B_lH_l^{(2)}(R) + C_lH_l^{(1)}(R)$, where $B_l$ and $C_l$ are also proportionality constants. The constants $A_l$, $B_l$, $C_l$, and $D_l$ must be set to enforce continuity of the field across the various boundaries, given by:

$$S(R) = \left\{\begin{array}{ll} A_lJ_l(m_1k_0r), & r \le b \\ B_lH_l^{(2)}(m_2k_0r) + H_l^{(1)}(m_2k_0r), & b < r \le a \\ D_lH_l^{(1)}(m_3k_0r), & r > a \end{array}\right\} \quad (10)$$

where we have set $C_l = 1$, and recall that $R = mkr$. A plot of $S(R)$ is the same as a radial amplitude plot of $E_z(R)$. Thus, for the TE polarization we have the following solutions for a dielectric cylinder:

$$\begin{aligned} E_r(R) &= 0 \\ E_\phi(R) &= 0 \\ E_z(R) &= S(R) \end{aligned} \quad (11)$$



We next write some fairly simple equations for the fields, which are given by the electromagnetic boundary conditions at each dielectric interface. These conditions state that the $E_z$, $H_r$, and $H_\phi$ fields (for the TE polarization) must be continuous. Since the electric field $E_z(r)$ has to be continuous across the boundaries, we obtain

$$\begin{aligned} \textit{boundary } 1: \quad & A_lJ_l(m_1k_0b) \\ & = B_lH_l^{(2)}(m_2k_0b) + H_l^{(1)}(m_2k_0b) \end{aligned} \quad (12a)$$

$$\begin{aligned} \textit{boundary } 2: \quad & B_lH_l^{(2)}(m_2k_0a) + H_l^{(1)}(m_2k_0a) \\ & = D_lH_l^{(1)}(m_3k_0a) \end{aligned} \quad (12b)$$

By analogy to a waveguide, Maxwell's equations require that $\partial E_z/\partial r - \partial E_r/\partial z = i\omega H_\phi$. Since $dE_r/dz = 0$ and the magnetic fields must be continuous on each side of the interface, the derivative $dE_z/dr$ must also be continuous across the interfaces. Thus:

$$\begin{aligned} \textit{boundary } 1: \quad & (m_1)A_lJ_l'(m_1k_0b) = (m_2)[B_lH_l^{(2)\prime}(m_2k_0b) \\ & + H_l^{(1)\prime}(m_2k_0b)] \end{aligned} \quad (13a)$$

$$\begin{aligned} \textit{boundary } 2: \quad & (m_2)[B_lH_l^{(2)\prime}(m_2k_0a) + H_l^{(1)\prime}(m_2k_0a)] \\ & = (m_3)D_lH_l^{(1)\prime}(m_3k_0a) \end{aligned} \quad (13b)$$

where the prime indicates the derivative of the Bessel function with respect to its argument. This notation is frequently used but can be confusing, so, for clarity we can write it explicitly:

$$J_l'(nkx) = \frac{d(J_l(mkx))|_{x\to a,\,b}}{mk \cdot dx} \tag{14}$$

Dividing Eqs. 13(b) by 12(b) gives

$$\frac{m_3 H_l^{(1)\prime}(m_3 k_0 a)}{m_2 H_l^{(1)}(m_3 k_0 a)} = \frac{B_l H_l^{(2)\prime}(m_2 k_0 a) + H_l^{(1)\prime}(m_2 k_0 a)}{B_l H_l^{(2)}(m_2 k_0 a) + H_l^{(1)}(m_2 k_0 a)} \tag{15}$$

where $B_l$ can be obtained by dividing Eqs. 13(a) by 12(a):

$$B_l = \frac{m_2 J_l(m_1 k_0 b) H_l^{(1)\prime}(m_2 k_0 b) - m_1 J_l'(m_1 k_0 b) H_l^{(1)}(m_2 k_0 b)}{-m_2 J_l(m_1 k_0 b) H_l^{(2)\prime}(m_2 k_0 b) + m_1 J_l'(m_1 k_0 b) H_l^{(2)}(m_2 k_0 b)} \tag{16}$$

These equations are equivalent to stating that a modified log-derivative function $u(r) = (1/k_0)((dE_z/dr)/E_z)$ holds continuous across any dielectric boundary, for the TE polarization.[46]

We need to find complex values for $k_0$ that are solutions of Eq. (15). There are, in fact, an infinite number of possible solutions corresponding to all the possible radial mode orders. Only the lowest-order modes (e.g., $n =$ 1–3) will typically be important since the higher orders are lossy and will not appear in the WGM spectra. This requires Eqs. (15) and (16) to be entered into a math package with a complex numerical root solver, such as Mathematica's "FindRoot" function. One fixes the desired angular number $l$ and the various capillary parameters, and enters a reasonably good guess for $k_0$ (e.g., $k_0 = l/(m_{\text{eff}}a)$) where $m_{\text{eff}}$ is an estimate of the effective refractive index for the mode. The root solver then completes the work.

Once the complex root $k_0$ has been found, the field (or its radial function) must be plotted in order to find which radial mode order the solution represents. In order to find the electric field profile, one must plot Eq. (10) using the value found for $k_0$ and the various cylinder parameters (radius $a$, film thickness $t$, and the refractive indices). The values of $A_l$, $B_l$, and $D_l$ must at this point be set to ensure that the field is continuous across the boundaries. The constant $B_l$ can be obtained from Eq. (16), once $k_0$ has been determined numerically, and then $A_l$ and $D_l$ are simply:

$$A_l = \frac{B_l H_l^{(2)}(m_2 k_0 b) + H_l^{(1)}(m_2 k_0 b)}{J_l(m_1 k_0 b)} \tag{17a}$$

$$D_l = \frac{B_l H_l^{(2)}(m_2 k_0 a) + H_l^{(1)}(m_2 k_0 a)}{H_l^{(1)}(m_3 k_0 a)} \tag{17b}$$

The field and the various coefficients will contain both real and imaginary parts. The way to deal with this for calculating the volume-integrated energy densities (which must be real) will be discussed later. The relative magnitude of the field is given by the absolute value:

$$|E_z| = \sqrt{(\text{Re}E_z)^2 + (\text{Im}E_z)^2} \tag{18}$$

and the intensity $I_z$ is proportional to $|E_z|^2$.

The radial functions for several different TE modes are shown for an LCORR and an FCM structure in Figure 3, from the solutions of Eq. (15). We can see some similarities and differences between the two structures. In the LCORR, the outer index is air; whereas in the FCM the glass capillary itself is the outermost material (the effects of the relatively remote outer wall seem to be measurable but are fairly minor).[47] Thus, in an LCORR the mode field is better confined toward the inner region of the structure, which is an advantage for sensing applications. In the FCM, the smaller index contrast between the fluorescent film and the capillary wall effectively "forces" the field further away from the channel.

For the TM polarization, we have the $H$-field along the cylinder axis, and the radial and azimuthal components of the magnetic field are zero. The Helmholtz equation is slightly different for this case. Assuming that $\varepsilon$ has no azimuthal dependence:

$$\nabla^2 H_z(r,\phi) - \frac{1}{\varepsilon}\frac{\partial \varepsilon}{\partial r}\frac{\partial H_z(r,\phi)}{\partial r} + k_0^2 m^2 H_z(r,\phi) = 0 \tag{19}$$

The second term simplifies to $-(2/m)\cdot(\partial m/\partial r)\cdot(\partial H_z/\partial r)$, which can be set to zero since we further assume no radial dependence of $m_1$, $m_2$, or $m_3$ within each of the layers. The result is therefore again a set of Bessel functions, this time specifically for $H_z$, and one can write



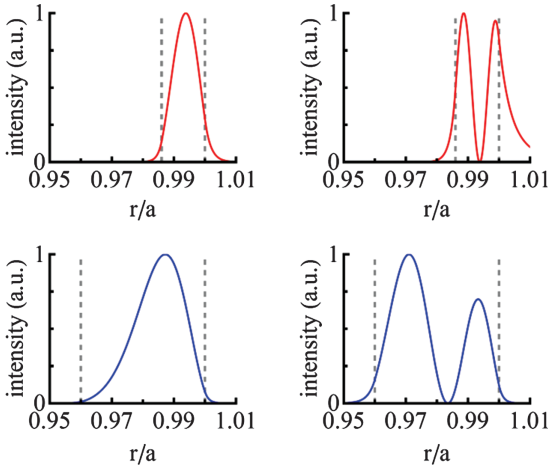


**Fig. 3.** First order (left) and second order (right) electric field profiles $S(R)$ for an FCM (top) and an LCORR (bottom). All modes have a resonance wavelength close to 800 nm. The LCORR outer radius was 50 $\mu$m and the wall was 2 $\mu$m thick. For the FCM, the inner radius was 50 $\mu$m and the fluorescent film was 0.7 $\mu$m thick, with a refractive index of 1.67. These values are close to typical experimental values for both structures. The dashed grey lines define the boundaries of the high-index layer.

a piecewise solution identical to Eq. (10) but with different coefficients:

$$T(R) = \begin{cases} a_l J_l(m_1 k_0 r), & r \le b \\ b_l H_l^{(2)}(m_2 k_0 r) + H_l^{(1)}(m_2 k_0 r), & b < r \le a \\ d_l H_l^{(1)}(m_3 k_0 r), & r > a \end{cases} \tag{20}$$

$T(R)$ is equivalent to the profile of $H_z(R)$. There can be both radial and azimuthal parts of the electric field, which can be written in vector form:[48]

$$\vec{E} = [E_r(R)\hat{r} + E_\phi(R)\hat{\phi}]e^{il\phi} \tag{21}$$

where, analogous to Eq. (11), we have

$$\begin{aligned} E_r(R) &= -\frac{1}{k_0 m^2}\frac{l}{r}T(mk_0 r) \\ E_\phi(R) &= -\frac{i}{k_0 m^2}\frac{d(T(mk_0 r))}{dr} \\ E_z(R) &= 0 \end{aligned} \tag{22}$$

In practice, we will only care about the first part of Eq. (22), since $E_r$ will be what we measure experimentally as the TM-polarized $E$-field.

The boundary requirements in this case are that $H_z$ and $E_\phi$ must be continuous. According to Maxwell's equations for the tangential field we have $\partial H_z/\partial r - \partial H_r/\partial z = i\omega m^2 E_\phi$. Similar to the previous case, $\partial H_r/\partial z = 0$, but since $E_\phi$ is continuous the derivative of the magnetic field $dH_z/dr$ must change by a factor of $m^2$ on crossing a boundary. At the dielectric interfaces, we therefore have:

$$\textit{boundary } 1: \quad (1/m_1)a_l J_l'(m_1 k_0 b) = (1/m_2)[b_l H_l^{(2)\prime}(m_2 k_0 b) + H_l^{(1)\prime}(m_2 k_0 b)] \tag{23a}$$

$$\textit{boundary } 2: \quad (1/m_2)[b_l H_l^{(2)\prime}(m_2 k_0 a) + H_l^{(1)\prime}(m_2 k_0 a)] = (1/m_3) d_l H_l^{(1)\prime}(m_3 k_0 a) \tag{23b}$$

Thus, we find another modified log-derivative function that must be continuous, given by $v(r) = (1/(k_0 m^2))((\partial H_z/\partial r)/H_z)$.

By setting the fields and the derivatives (divided by $m^2$) continuous across the interfaces we obtain:

$$\frac{m_2 H_l^{(1)\prime}(m_3 k_0 a)}{m_3 H_l^{(1)}(m_3 k_0 a)} = \frac{b_l H_l^{(2)\prime}(m_2 k_0 a) + H_l^{(1)\prime}(m_2 k_0 a)}{b_l H_l^{(2)}(m_2 k_0 a) + H_l^{(1)}(m_2 k_0 a)} \tag{24}$$

and

$$b_l = \frac{m_1 J_l(m_1 k_0 b) H_l^{(1)\prime}(m_2 k_0 b) - m_2 J_l'(m_1 k_0 b) H_l^{(1)}(m_2 k_0 b)}{-m_1 J_l(m_1 k_0 b) H_l^{(2)\prime}(m_2 k_0 b) + m_2 J_l'(m_1 k_0 b) H_l^{(2)}(m_2 k_0 b)} \tag{25}$$

Equations (24) and (25) are solved in the same way as (15) and (16).

Equation (20) is often called the transverse magnetic "radial function" $T(r)$, which describes the magnetic field $H_z$. For the TM situation, one will usually be measuring only $E_r$; that is, the electric field pointing along the radial direction. The continuity of the electric displacement, $\varepsilon E_r$, implies that there will be a jump or discontinuity in the electric field across each boundary for this polarization,[49] as can be seen in Eq. (22). Thus, once the coefficients in Eq. (20) have been determined, the electric field profile $E_r(r)$ has to be adjusted by the ratio of the dielectric constant for each layer, as illustrated in Figure 4 for $[E_r(r)]^2$.

In order to visualize the WGM field around the capillary's cross section, we need to consider the azimuthal part of Eq. (1), given by by $e^{\pm il\phi}$. Multiplication of the radial function by $e^{\pm il\phi}$ gives a rotating wave pattern for regions where $r < \sim l/k$, in the region dominated by $J_l(m_1 kb)$. However, as can be seen in Eq. (9), the Hankel functions have an $e^{ikr}$ dependence which becomes obvious at large $r$. This results in radial dependence of the phase, which, combined with the azimuthal one, forms a spiral pattern in the regions where $r > \sim l/k$, within which the Hankel functions dominate the radiation pattern (Fig. 5). The sense of the spiral (clockwise or counterclockwise) depends on the sign of $e^{\pm il\phi}$.

Finally, the time dependence of the field is included by replacing $e^{\pm il\phi}$ with $e^{i(\pm l\phi - ckt)}$. In this way, "movies" of the WGM field can be produced. Since the Hankel function has the asymptotic form $e^{i(mkr + l\phi - l\pi/2 - \pi/4 - ckt)}$ (e.g., for counterclockwise rotation), we can see from Eq. (9) that increasing $t$ must be balanced by increasing $r$ (for constant $l\phi$) in order to obtain a wavefront of constant phase. The wave spirals outward in time, with the real and imaginary parts phase shifted by $\pi/2$. These radiating waves are the solutions for LCORRs, which are pumped



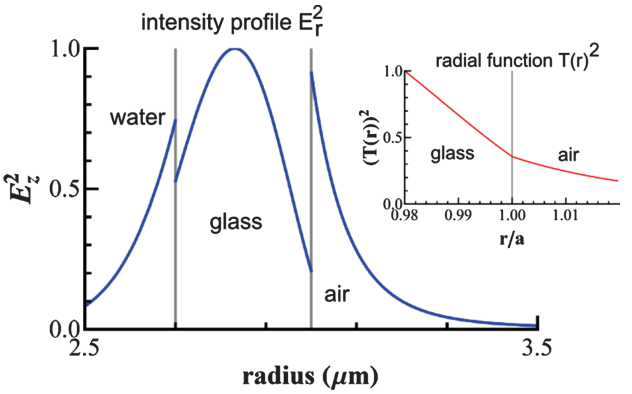


**Fig. 4.** The TM-polarized electric field intensity $[E_r(r)]^2$, for a disk with $a = 3$ $\mu$m, $b = 2.7$ $\mu$m, and refractive indices $m_1 = 1.33$, $m_2 = 1.45$, and $m_3 = 1.00$, with $l = 35$ and $\lambda_0 = 660.179$ nm. There are discontinuities in the relative intensity across the boundaries. The inset shows the radial function $[T(r)]^2$ at the outer boundary (Eq. (20)), showing the continuity of the function and the change in the slope at the glass-air boundary.

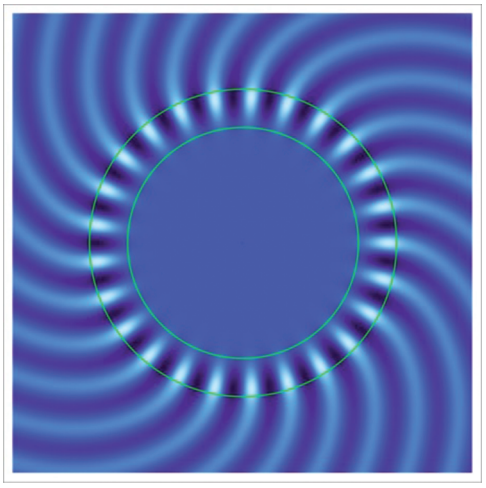

**Fig. 5.** Plot of the field amplitude for a counterclockwise-propagating first-order WGM in a layered disk with $m_1 = 1.45$, $m_2 = 1.67$, and $m_3 = 1.33$, TE polarization. The spiral structure in the outer region is a result of the Hankel function. The non-rotating fields shown in Figure 1 are the superposition of clockwise and counterclockwise modes.

evanescently via a tapered fiber. For FCMs, the interference of the clockwise and counterclockwise-propagating waves yields stationary standing wave patterns like those in Figure 1.

One frequently finds Eq. (7) cast into a quantum-mechanics-like format with a "potential energy" term that, by analogy, can provide additional insights into the properties of the resonances and the mechanisms by which light is transferred (or "tunnels") from the boundary of a cylinder or sphere toward the outside region.[41,46,50,51] For the case of cylinders, the relatively straightforward method to obtain a Schrodinger-like equation is clearly shown in Ref. [50]. However, these formats are not necessary in order to be able to calculate and plot the WGM fields.



## 4. MODE CHARACTERISTICS

The WGM $Q$ factors can be directly calculated from the equations in the previous sections. The real part of $k_0$ gives the resonance wavelength $\lambda_0 = 2\pi/\mathrm{Re}[k_0]$ and the mode quality factor $Q = Re[k_0]/(2\mathrm{Im}[k_0])$ of the mode. Assuming no material-related losses, then the $Q$ factors are controlled only by radiative losses and are mainly governed by the refractive index contrast between the confining layer and the outer material, the thickness of the layer, and the diameter of the capillary. As shown in Figure 2, the large index contrast between the outer capillary wall and outside air (1.45 vs. 1.00), as compared to a typical fluorescent layer and the inner wall (e.g., ~1.6 vs. 1.45) lead to larger $Q$ factors for the LCORR as compared to the fluorescent-type structures. For typical LCORR parameters, the calculated WGM $Q$ factors can be enormous (e.g., $> 10^{15}$ for the first-order radial modes of a 100-$\mu$m-diameter capillary). Since experimental observations give $Q = 10^6$–$10^7$ for structures in this size range,[52] other effects such as scattering or absorption must limit the ultimate achievable $Q$ factor. For FCMs, the calculated $Q$ factors are typically in the range of $10^3$–$10^6$ depending on the film thickness, whereas experiment gives $Q \approx 10^3$.[53] For both structures, the higher radial orders are generally lossier and tend to have lower $Q$, as long as there are no material-related losses.

Material losses can also be modeled by using a complex refractive index in the equations shown in the previous section. These losses lower the achievable $Q$ factor, which could in fact be a sensing transduction mechanism in some cases.[54] The total $Q$ factor is related to the various loss parameters according to $1/Q_{\mathrm{total}} = 1/Q_{\mathrm{rad}} + 1/Q_{\mathrm{abs}} + 1/Q_{\mathrm{sca}} \ldots$, where $Q_{\mathrm{rad}}$, $Q_{\mathrm{abs}}$, and $Q_{\mathrm{sca}}$ are the radiation limited, absorption limited, and scattering limited $Q$ factors, respectively. Which loss effect dominates depends on the size and structure of the resonator: for small or high curvature structures, $Q_{\mathrm{rad}}$ is usually the limiting parameter, whereas for large ones material absorption or scattering represent the ultimate limit.[55,56] Figure 6 illustrates the effect of absorption in the analyte, assuming the typical device parameters given in the figure caption.[47]

In an LCORR, the free spectral range (FSR: the frequency spacing between modes), finesse (the ratio of the mode spacing to the mode width), and visibility (a measure of mode intensity compared to the background) are rarely measured experimentally, since the tunable laser measurements are typically done over a range much smaller than one FSR. In an FCM, data is simultaneously collected over a range of wavelengths much larger than the FSR, so the periodicity in the WGM spectrum should be easily observable (e.g., Fig. 7). This can be beneficial for detecting small shifts for sensing applications; for example, by using Fourier methods to measure the resonance shifts over the whole spectrum rather than using just one peak.[57,58]

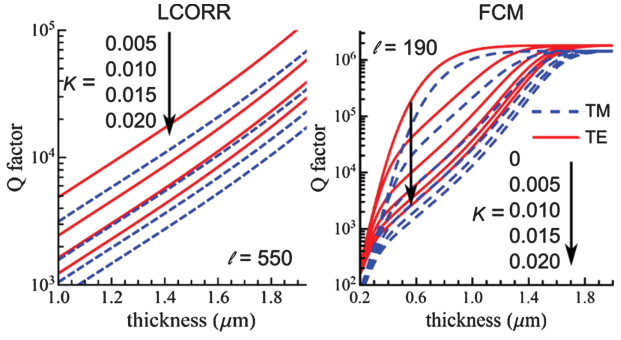


**Fig. 6.** Effect of absorption or scattering losses in the analyte, for an LCORR (left) with $a = 50$ $\mu$m and an FCM (right)[47] with $a = 15$ $\mu$m, as a function of the confining layer thickness (index $m_2 = 1.45$ for the LCORR and 1.67 for the FCM). The outer layer $m_3$ was either air (LCORR) or glass with $m_3 = 1.45$ (FCM), and the channel index $m_1 = 1.33$. For the LCORR, the $Q$ factors are so high in the absence of all but radiation losses that the $\kappa = 0$ case (no material losses) is not shown. The outer capillary radius of the LCORR was 50 $\mu$m, the same as the inner capillary radius of the FCM.

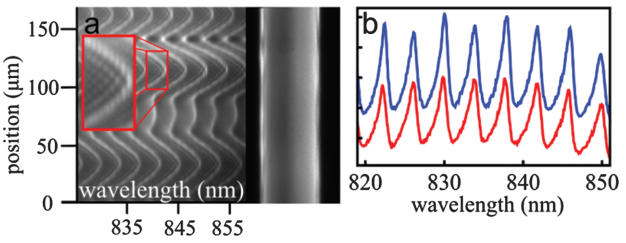


**Fig. 7.** (a) TM-polarized spectral-spatial mode map along the length of the capillary shown in the fluorescence image on the right side of panel (a). The variations in the resonance wavelengths are due to changes in the fluorescent silicon quantum dot film thickness along the length of the capillary. The substructure in the zoomed-in region (red box) is due to spiraling modes. (b) shows representative "1 dimensional" spectra for water (blue) and ethanol (red) in the channel. Modified From [47]. S. Lane, J. Chan, T. Thiessen, and A. Meldrum, Whispering gallery mode structure and refractometric sensitivity of fluorescent capillary-type sensors. *Sensors and Actuators B: Chemical* 190, 752 (**2014**).

## 5. SENSITIVITY AND DETECTION LIMITS

### 5.1. Calculating the Refractometric Sensitivity

There are several related ways to calculate the sensitivity to changes in the channel index. Perhaps the simplest one starts by noting that the resonant wavelength is approximately given by

$$\lambda_0 \approx \frac{2\pi a}{l}(f_1 m_1 + f_2 m_2 + f_3 m_3) \tag{26}$$



Here, $f_i$ is simply the fraction of the mode energy in the $i$th layer and the term in the brackets is the average refractive index, $a$ is the capillary radius, and $l$ is the angular mode number. Taking the derivative yields

$$S = \frac{d\lambda}{dm_1} \approx \frac{2\pi a f_1}{l} \approx \frac{\lambda_0 f_1}{m_2} \tag{27}$$

where it is assumed that all of the light is in layer 2 so that $l \approx 2\pi m_2 a/\lambda_0$. Obviously this approximation is crude, but it does give a reasonable estimate of the sensitivity, as we will show below.

Alternatively, the sensitivity can be calculated in a more fundamental way:

$$S = \frac{d\lambda}{dm_1} = \frac{-2\pi(dk/k_0^2)}{dm_1} = -\frac{\lambda_0}{dm_1}\cdot\frac{dk}{k_0} \tag{28}$$

Here, $dk/k_0$ is the fractional shift in the magnitude of the wavevector induced by a small change in the refractive index $m_1$. Teraoka and Arnold[59–61] showed for a layered microsphere that this fractional shift depends on the fraction of the mode energy within the analyte. They also showed how to estimate the fractional shift using perturbation theory:

$$\frac{dk}{k_0} = -\frac{1}{2}\frac{\int_{V_p}\partial\varepsilon_r\vec{E_0^*}\cdot\vec{E_p}d^3r}{\int_V \varepsilon_r\vec{E_0^*}\cdot\vec{E_0}d^3r} \tag{29}$$

in which $\vec{E_0}$ and $\vec{E_p}$ represent the initial electric field and the one perturbed by the index change in the channel, respectively. The denominator is integrated over all space ($V$) while the numerator reflects the volume $V_p$ in which the dielectric constant has been changed by $d\varepsilon$ (the inner layer).

We showed how to solve these integrals in Ref. [62], yielding the following equations for the refractometric sensitivity of capillary structures:

$$S_{TE} = \frac{\lambda_0}{m_1}\cdot\frac{I_1}{I_1+I_2+I_3} \tag{30a}$$

$$S_{TM} = \lambda_0\frac{(2k_1^2)}{m_1^3(k_0^2+(k_0^*)^2)} \cdot\left(b|a_l|^2\left(\frac{dJ_l^*(m_1k_0r)}{dr}\Big\|_b J_l(m_1k_0b)+J_l^*(m_1k_0b) \times\frac{dJ_l(m_1k_0r)}{dr}\Big\|_b\right)+\frac{k_0^2+(k_0^*)^2}{k_{0,1}^2}I_1\right) \cdot\left(\left[\frac{I_1}{m_1^2}+\frac{I_2}{m_2^2}+\frac{I_3}{m_3^2}\right]\right)^{-1} \tag{30b}$$

where the "$I$" terms represent the volume-integrated electric field energy within layers 1, 2, or 3, the "$*$" indicates the complex conjugate, and $(k_{0,1}, k_{0,2})$ are the (real, imaginary) parts of the resonance wavevector.

The energy terms can be obtained by numerically integrating the following expressions:

$$I_1 = \int_0^{m_1k_{0,1}b} x|A_lJ_l(\tilde{x})|^2\,dx \tag{31a}$$

$$I_2 = \int_{m_2k_{0,1}b}^{m_2k_{0,1}a} x|B_lH_l^{(2)}(\tilde{x})+H_l^{(1)}(\tilde{x})|^2\,dx \tag{31b}$$

$$I_3 = \int_{m_3k_0a}^{\infty} x|D_lH_l^{(1)}(\tilde{x})|^2\,dx \tag{31c}$$

where $\tilde{x} \equiv x(1+ik_{0,2}/k_{0,1})$ and $x \equiv k_{0,1}nr$. Equation (31) is written explicitly for the TE case; for the TM polarization one replaces the $A_l$, $B_l$, $D_l$ coefficients with the TM ones. Equation (31) can require some care in setting the integration limit, since in practice Eq. (31c) diverges, although the divergence might not always be apparent up to an integration limit close to $Qa$. For low $Q$-factors, the field may never approach zero outside the outer boundary, which will lead to further issues in setting the integration limit.

For biosensing applications, the refractive index changes will be localized to the region immediately at the capillary inner wall. In that case one does not have a uniform change in the refractive index, as assumed in the previous equations, and the sensitivity does not have the same meaning (since there is effectively no $dm_1$). Teraoka and Arnold showed how the resonance shift related to a uniform layer of adsorbed particles can be calculated.[60,61] Equation (30)

becomes slightly modified, since one instead has to calculate the shift due to a uniform density of small particles of index $n_p$ coated on the channel surface. For a uniform refractive shift, Zhu et al.[63] showed that the fractional shift due to biomolecular absorption can be estimated as:

$$\frac{d\lambda}{\lambda} = \sigma_p \alpha_{ex} \frac{2\pi\sqrt{m_2^2 - m_1^2}}{\varepsilon_0 \lambda_0^2} \frac{m_2}{m_1^2} S \tag{32}$$

where $\varepsilon_0$ is the vacuum permittivity, $\sigma_p$ is the biomolecule surface density, $\alpha_{ex}$ is the biomolecule's excess polarizability, and $S$ is the sensitivity calculated previously. The fractional shift depends linearly on the device sensitivity and the concentration of surface particles.

### 5.2. Detection Limits: Getting the Most Out of the Measurement

The detection limit (DL) is the most important figure of merit for microfluidic capillary sensors. The DL depends on the sensitivity of the device and the wavelength shift resolution limit, $\Delta\lambda_{min}$, of the measurement system, and is given by

$$\mathrm{DL} = \Delta\lambda_{min}/S \tag{33}$$

in dimensionless units. A low detection limit requires a small shift resolution limit and a large sensitivity. Two different methods can be used to sense the resonance shift.[64,65] In the "intensity-shift" method, the transmission is measured through a waveguide or fiber taper, evanescently coupled to the device, at a fixed wavelength. The laser should be tuned to the maximum slope of the WGM and the shifts are measured as intensity changes. This method can be very sensitive but it has a small dynamic range for changes in the capillary channel index. In the wavelength-shift method, a tunable laser is scanned across a resonance and the peak shift is measured.

In one approximation, the wavelength shift resolution was considered inversely proportional to the $Q$ factor and sensitivity of the WGM, such that DL $\alpha$ $(QS)^{-1}$.[66] Unfortunately, this leads to some inconsistency in the literature, with different works assuming various wavelength shift resolutions as fractions of the resonance linewidth.[67] Several subsequent works have assumed that the detection limit is inversely related to the $Q$ factor. However, these assumptions are too simplified; good detection limits can also be achieved with low $Q$ factors, depending on the data sampling, noise levels, and data analysis methods.[57,68]

If the peak wavelengths are to be found via Lorentzian curve fitting, Silverstone et al.[57] used numerical modeling to find $\Delta\lambda_{min}$ over a fairly wide range of experimental conditions, within a $3\sigma$ level of certainty:

$$\Delta\lambda_{min}(3\sigma) = \frac{2.2 \cdot 10^{-20} \cdot \Delta f^{0.29} \cdot P^{0.65}}{SNR^{0.51}} \text{ meters} \tag{34}$$

Here, $\Delta f$ is the width of the WGM in units of Hz (which can be directly converted from wavelength via $|\Delta f| = |c\Delta\lambda/\lambda^2|$), $P$ is the sampling rate also in Hz (i.e., spectral frequency range per pixel on the CCD), and the SNR is on a linear scale. The $Q$ factor does play a role via $\Delta f$ but it is a rather weak effect (i.e., changing the linewidth by three orders of magnitude only changes the $3\sigma$ resolution $\Delta\lambda_{min}$ by a factor of ~7.5), holding everything else constant and assuming that the sampling rate is greater than the Nyquist rate.

For an FCM, the spectrometer will typically collect data over a range of wavelengths much larger than the FSR. Silverstone et al. found that this case lends itself naturally to Fourier analysis techniques. Accordingly, they applied the Fourier shift theorem over the periodic WGM spectrum to find the wavelength shifts induced by different analytes in the channel. A numerical analysis over a wide range of conditions showed that the detection limit is only very weakly (and inversely) dependent on the linewidth:[57]

$$\Delta\lambda_{min}(3\sigma) = \frac{1.75 \cdot 10^{-14} P^{0.50}}{\Delta f^{0.12} \cdot SNR^{0.52}} \text{ meters} \tag{35}$$

Here, increasing the $Q$ factor (i.e., decreasing the WGM linewidth) by a factor of 1000 worsens the wavelength resolution by a factor of about 2.3, as long as the linewidth remains smaller than the FSR. Essentially, higher $Q$ leads to poorer sampling of each peak and ultimately decreases the ability to resolve spectral shifts.



## 6. EXPERIMENTAL TECHNIQUES (FABRICATION, FUNCTIONALIZATION, EXCITATION, AND ANALYSIS)

Experimental details for making LCORR and FCM sensor measurements are rarely included in standard publications where only a short experimental section is typically given. Fortunately, two experimental papers have been published, that focused on the laboratory aspects of LCORRs[69] and FCMs.[70] Essentially, the experimental aspects can be broken down into three parts.

### 6.1. Sample Fabrication

Making an LCORR or FCM is non-trivial. LCORRs are usually synthesized by a combination of heating and pulling, and etching with hydrofluoric acid. The heating and pulling technique can be adapted from custom-built fiber tapering stations. These often use a hydrogen torch or $CO_2$ laser to locally heat the sample, which is simultaneously stretched by attaching the sample to small servo motors on each side. Typically, a bank of "recipes" for the temperature, time, and pulling rate has to be custom built to produce the desired structure, which takes some amount of trial and error.

A problem with the LCORR is that there will be uncertainty in the capillary wall thickness unless the recipes are well characterized and reproducible. Since the overall sensor performance is highly sensitive to the wall thickness,

further thinning to a desired value is often done by pumping HF through the channel while monitoring the optical response of the capillary. This obviously requires the use of dangerous chemicals and is one of the drawbacks to LCORR fabrication. However, an advantage is that the wall thickness can be controlled quite precisely. The final capillary is extremely fragile and a considerable amount of care is required in handling it.

With FCMs, the biggest fabrication difficulty is making a uniform luminescent film of the right thickness inside the capillary. Both silica-embedded quantum-dot[71] and dye-doped polymer films[58] have been synthesized. McFarlane et al.[70] reported that the success rate is quite low (on the order of a few percent) and is sensitive to the age of the chemicals, due to oxidation and hydration issues. The film thickness is difficult to control, although finer tuning could likely be obtained, for example by etching the layer containing the QDs. Rolled "tube" FCMs are another alternative,[72] but these are difficult to interface to a pumping system.

### 6.2. Setup

Once the sample has been fabricated, the next issue is getting it hooked up to a syringe pump and associated tubing system. Norland-type adhesive (e.g., #76) yields good results on polyethylene tubing and standard solvents such as methanol, ethanol, water, or phosphate buffer solutions, but it appears at least partly dissolved by acetone. Typically, tests need to be conducted to ensure that the adhesive is compatible with the tubing and solvent used, otherwise the seal between the tubing and the capillary can weaken and eventually begin to leak. The tubing length should be minimized in order to avoid the experiment taking a long time as the solvents are slowly pumped through long tubing lengths. A pumping rate of a few microLitres per minute or less is typical, using a standard syringe pump.

### 6.3. Data Collection

For an FCM, the only requirement is a system to collect and analyze the luminescence. A microscope objective coupled to a simple spectroscopy system such as the SGS from the Santa Barbara Instruments Group (now no longer produced) or the LHires from Shelyak work well. The WGM spectrum can be collected over a wide range of wavelengths much larger than the free spectral range. Thus, many modes are collected at the same time, although at the cost of a relatively low signal. For an LCORR, a tapered fiber must be fabricated and brought near the capillary wall using piezo-controllers. Then light from a tunable laser is coupled into the taper and scanned across one or more WGM resonances. Alternatively, the LCORR can be interfaced to a system of optical waveguides on a chip.[73] The WGMs appear as dips in the transmission spectrum collected by a photodiode at the opposite end of the taper. The signal-to-noise ratio is much higher for a given collection time than for the fluorescence method, but the wavelength range that can be collected is narrower.

Each technique has a specific set of advantages and disadvantages. The LCORR is considerably more difficult and expensive to analyze, but it yields better detection limits as compared to the FCM, which in turn is far more durable and robust.

## 7. PITFALLS

### 7.1. Thermal Effects

One of the biggest issues with capillary-based WGM sensors is thermal drift. Temperature fluctuations in the laboratory, or as a result of absorption of the pump light, modify the refractive index of all three layers via the thermo-optic effect. Thermal expansion can also affect the resonant wavelength. For example, in an FCM the resonant wavelength was found to shift by around 1 pm/mW of laser power used to excite the fluorescent layer.[71] Considering that shifts as small as 1 pm can theoretically be detected via Fourier methods, temperature fluctuations may represent the ultimate barrier toward achieving lower detection limits. In LCORRs, laboratory temperature drifts as small as 1–2 K can be significant.[74]

The magnitude of the temperature-induced wavelength shift can be obtained by noting that a change in the effective index or capillary radius produces a proportional change in the resonant wavelength, which can be assumed linear. Thus, $d\lambda/\lambda_0 = dn_{\text{eff}}/n_{\text{eff}} + da/a$. If these changes are temperature-dependent, we can divide both sides by $dT$, yielding

$$\frac{d\lambda}{dT} = \lambda_0\left(\frac{1}{m_{\text{eff}}}\frac{dm_{\text{eff}}}{dT} + \frac{1}{a}\frac{da}{dT}\right) \tag{36}$$

The second term on the right side in the brackets is the linear thermal expansion coefficient of the capillary, $\alpha$, and $m_{\text{eff}}$ is approximated by $f_1 m_1 + f_2 m_2 + f_3 m_3$, with $f_i$ being the energy fraction in the $i$th layer. Using the expressions derived above for the fractional intensities, the temperature-induced wavelength shifts for both polarizations is:

$$\frac{d\lambda_{\min,\,TM}}{dT} = \lambda_0\left(\frac{(I_1/m_1^2)\kappa_1 + (I_2/m_2^2)\kappa_2 + (I_3/m_3^2)\kappa_3}{I_1/m_1 + I_2/m_2 + I_3/m_3} + \alpha\right) \tag{37}$$

$$\frac{d\lambda_{\min,\,TE}}{dT} = \lambda_0\left(\frac{I_1\kappa_1 + I_2\kappa_2 + I_3\kappa_3}{m_1 I_1 + m_2 I_2 + m_3 I_3} + \alpha\right) \tag{38}$$

where the thermo-optic coefficient in the $i$th layer is $\kappa_i = d\lambda/dT_i$. Finally, the temperature-shift-induced detection limit can be found by multiplying Eq. (33) by $dT/dT$:

$$\text{DL}_{\text{thermal},(TE,\,TM)} = \frac{d\lambda_{\min,\,(TE,\,TM)}}{dT}\cdot\frac{dT}{S_{TE,\,TM}} \tag{39}$$

The term $dT/S$ is the ratio of the thermal fluctuation in the experiment to the sensitivity of the sensor. Equation (39) is the refractometric detection limit due to temperature fluctuations alone. The overall detection limit is

then the sum of the resolution-limited one (Eq. (33)) and temperature-limited one (Eq. (39)).

Figure 8 shows the temperature-fluctuation-based detection limits for an FCM and an LCORR, assuming a laboratory fluctuation of 1 K. For different temperature fluctuations, the results scale proportionally. For an FCM, a zero thermal detection limit can be achieved for a sufficiently thin film (e.g., ~400 nm as in Fig. 8), but for more typical thicker films, a low DL requires either a large negative thermo-optic coefficient or a large refractive index of the solvent. This is because only a relatively small fraction of the mode energy extends into the channel. For an LCORR, a wall thickness of ~1.3 $\mu$m can produce a zero thermal DL within the range of $m_1$ and $\kappa$ of typical solvents such as water, for the first order mode. The optimal wall thickness depends on the radial mode order to be measured.

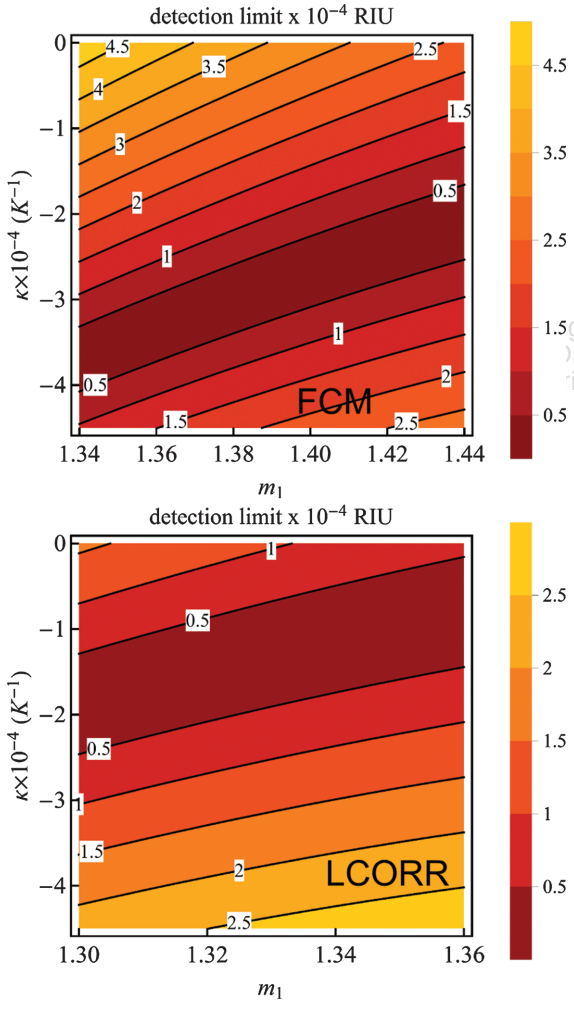


**Fig. 8.** Contour maps of the thermal detection limit for a typical FCM (top) and LCORR (bottom), as a function of the refractive index (abscissa) and thermo-optic coefficient (ordinate) of the analyte. FCM: first radial order, TE polarization, $l = 190$, $a = 15$ $\mu$m, fluorescent layer thickness $t = 0.4$ $\mu$m, and $m_2 = 1.67$. LCORR: first radial order, TE polarization, $l = 550$, $a = 50$ $\mu$m, wall thickness $t = 1.3$ $\mu$m, $m_2 = 1.45$. Both structures can theoretically achieve a zero thermal limit (inside the dark red band) under normal conditions if the wall thickness can be controlled precisely.

Two papers recently showed that there can be an optimum thickness at which the thermo-optic coefficient of the silica-based layer 2 can be balanced by the negative coefficient of water, leading to a zero net thermal shift.[74,75] For this specific thickness, the thermal detection limit (Eq. (39)) becomes zero. These zero drift "valleys" are within the dark red bands for the two specific examples shown in Figure 8. In the case of an FCM, getting a $DL_{thermal} = 0$ depends on having a very thin fluorescent coating. In many practical cases, the thermal drifts can represent the ultimate detection limit of the device.

### 7.2. Mechanical Drift

A second aspect that can limit the achievable DL is mechanical drift. In the case of an LCORR, mechanical instabilities can lead to relative motion between the fiber taper and the capillary. Since the taper must be held very close to the LCORR in order to have efficient coupling, the taper drift can affect the $Q$ factor and resonant wavelength of the device. In the simplest approximation, the gap-dependence of the linewidth has been approximated as[76]

$$\delta\lambda = \frac{\lambda_0}{Q_0}\left(1 + \frac{\gamma_e}{\gamma_0}\right) \tag{40}$$



Here, $Q_0$ is the "intrinsic" $Q$ factor (in the absence of the taper), $\gamma_e$ is the taper-to-disk coupling rate, and $\gamma_0$ is the cavity's intrinsic loss rate, which is simply $2\pi c/(\lambda_0 Q_0)$. The value of $\gamma_e$ depends exponentially on the gap: $\gamma_e = \gamma_e(0)e^{-\eta g}$, where $\gamma_e(0)$ is the coupling rate when the cavity and the taper are in contact, $\eta$ describes the strength of the coupling, and $g$ is the gap distance. These values need to be obtained experimentally; for GaAs nanodisks with a silica fiber taper, $\eta$ was found to be 0.0025 nm$^{-1}$ and $\gamma_e(0) \approx 15$ GHz. Typically, the linewidth may change by a few hundred pm upon changing the gap distance from 350 to 200 nm, at an increasing rate as the gap narrows.[77] In the case of intensity-shift sensor transduction, the transmission at a fixed wavelength also depends on the taper-cavity distance via[78]

$$T = \left(\frac{1 - \gamma_e\gamma_0}{1 + \gamma_e\gamma_0}\right)^2 \tag{41}$$

In an LCORR, taper-capillary drift can cause small wavelength shifts. While the magnitude of such shifts as a function of gap cannot be readily calculated, redshifts up to 8 nm have been reported for low-angular-order WGMs of silicon microdisks,[79] while other theoretical studies have suggested a more complicated gap dependence.[80] In LCORRs, the drift-induced wavelength shifts are probably quite small and likely do not appreciably affect the detection limits as much as thermal drifts or the wavelength shift resolution limits.

For FCMs, the main issue is mechanical drift with respect to the entrance slit of the spectrometer. While this effect cannot easily be quantified, we have found that mechanical motion of the capillary or the microscope stage itself can, over a period of hours, significantly affect the results. If the capillary axis is aligned perpendicular to the entrance slit, any drift perpendicular to the capillary axis (i.e., along the length of the slit) will change the vertical position of the spectral image on the CCD array. This can lead to data processing and wavelength calibration issues. Parallel drift (along the capillary channel) means that a slightly different part of the capillary is exposed in each image. Unless the capillary parameters (i.e., film thickness and inner diameter) are uniform along the length of the drift, artificial shifts will appear in the sensorgrams.

### 7.3. Spiral Modes

A third effect (after thermal fluctuations and drift) is more closely related to the physics of capillary WGMs. All of the calculations in the previous section assumed that there was no $z$-component of the electric field (i.e., $k_z = 0$ along the capillary axis). However, both LCORRs and FCMs can show strong spiraling mode effects.[81] Spiral, or "skew," modes are well known in optical fibers[82] and have been described with respect to cylindrical WGMs.[84] For small spiraling angle $\theta$ (Fig. 9), the resonance wavelength can be estimated as[82]

$$\lambda \approx \frac{\pi a}{l}\left(2m_{\text{eff}} - \frac{\theta^2}{m_{\text{eff}}}\right) \tag{42}$$

Equation (42) shows that spiral modes should appear on the short-wavelength side of the main WGM.

Spiral modes can appear as a set of peaks that ride on the short-wavelength tail of the main WGMs. Whether these peaks are resolvable or simply appear as a short-wavelength skewing of the main WGM seems to depend on the experimental conditions, such as the thickness of the confining layer.[83] A key aspect has to do with angular distribution of the illumination. In the case of LCORRs, Zamora et al.[84] showed that the excitation of the spiral modes could be controlled to some degree by the taper diameter. Wider tapers produce a narrow angular distribution of the excitation light, and were found to reduce the appearance of spiral modes. The drawback is, of course, that the coupling rate decreases due to the smaller evanescent extension of the field for a thicker taper. In the case of FCMs, the luminescence is mainly isotropic (to a first approximation ignoring Purcell effects) regardless of the excitation condition, and therefore spiral mode skewing of the main WGMs is ubiquitous and unavoidable.

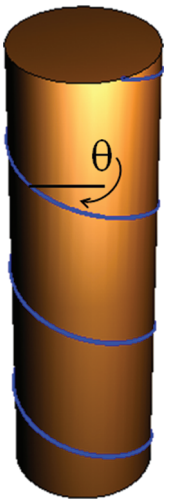


**Fig. 9.** Diagram showing ray path of a spiral WGM (blue line). The angle $\theta$ is used to calculate the associated resonance wavelength using Eq. (42).

The presence of spiral modes can have minor detrimental effects on the sensing performance, since it essentially broadens and skews the WGMs. If the WGMs become skewed, they cannot be modeled using a Lorentzian lineshape. Thus, if one wants to use curve fitting methods to measure peak shifts, one needs a function that can adequately describe the skewed mode shape. Manchee et al.[71] showed that the following "skewed Lorentzian"[85] equation fits the WGMs quite well, although it lacks physical basis with respect to WGMs:

$$P(f) = \frac{2A}{\pi\gamma(f)} \Big/ \left[1 + 4\left(\frac{f - f_0}{\gamma(f)}\right)^2\right] \tag{43}$$



Here, $f_0$ is the central frequency, $A$ is a normalizing factor, and the peak width $\gamma$ describes the frequency-dependence of the skewing according to

$$\gamma(f) = \frac{(1+B)\gamma_0}{1 + B \cdot e^{c(f-f_0)}} \tag{44}$$

where $c$ is another fitting parameter.

## 8. EXAMPLES OF RELEVANT SENSORS

Several potential sensor applications have been explored and experimentally verified. Most of the work has focused on LCORRs, since these structures have been studied for a longer time and by more research groups. This is not meant as an exhaustive sampling of all such work, but simply as a brief overview to illustrate the almost limitless possibilities of refractometric capillary-based biosensing. Some studies show physical versatility of these systems, which are able to handle almost any solvent including viscous, dense oils,[86] and in many cases true chemical biosensing has been demonstrated.

The most common channel wall functionalization scheme so far is based on the standard silanization reaction.[87,88] This starts with a clean, –OH-terminated surface, which can be obtained by HCl washing followed by rinsing with methanol, water, or other alcohols, or by annealing in a hydrogen- or moisture-rich ambient, or other preparation methods.[89] The next step is typically to pump

an amine-terminated silane solution (e.g., aminopropyltri(m)ethoxysilane: APT(M)S or APT(E)S) into the capillary. The $CH_3$ end of the APTS molecule hydrolizes with water, forming an OH termination which then binds with –OH terminated silica surface to bind the silane through an Si–O–Si link, producing another water molecule in the process (Fig. 10).

This reaction is sensitive to the water concentration;[90] even 1–2% water in the APTS in (m)ethanol solutions can cause extensive polymerization of the APTS and the formation of an uneven and non-uniform functionalized surface. Such surfaces tend to be unstable and susceptible to the subsequent undesired removal of "chunks" of poorly-bound polymerized material. Anhydrous functionalization can be desirable if enough water to maintain the reaction is available from the surface reaction. Ideally, the resulting surface would consist of a monolayer of APTS on the channel wall, with the $–NH_2$ terminus available for reaction, but this can be difficult to achieve on a consistent basis.[91]

Some of the earliest examples with LCORRs involved single-strand DNA sensing.[92,93] Single-stranded (or double stranded)[94] DNA fragments can bind to the amine-terminated silanized surface layer. Detection limits were found to be on the order of 4 pg per square millimeter of the channel surface, corresponding to a density of about $10^{10}$ molecules/cm$^2$ for an LCORR with a sensitivity of about 37 nm/RIU, which is high for a first-order WGM. The same group later demonstrated the binding of double-stranded DNA to methyl binding proteins,[95] rather than using the silane-binding schemes discussed in the previous paragraph.

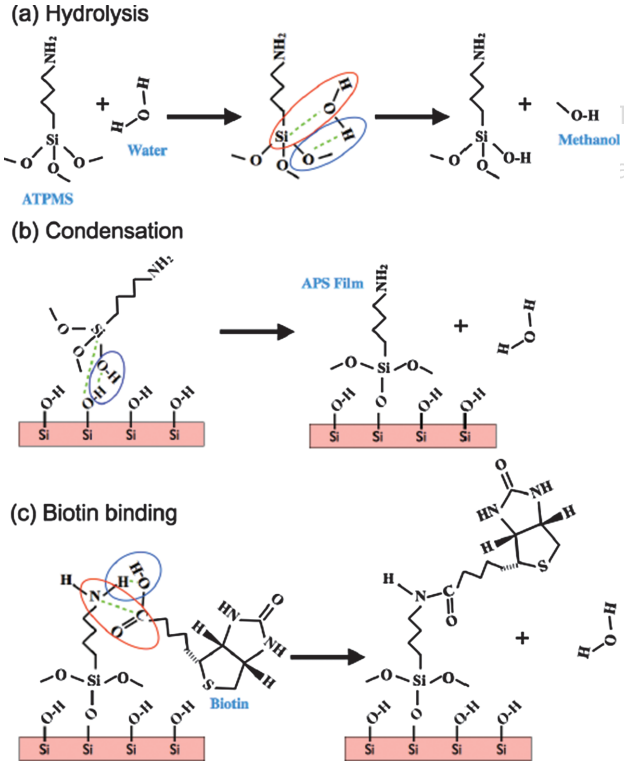


**Fig. 10.** Silanization scheme illustrating surface silanization (hydrolysis and condensation steps), followed by binding of biotin to the silanized surface. Modified From [101], N. A. Lapin and Y. J. Chabal, Infrared characterization of biotinylated silicon oxide surfaces, surface stability, and specific attachment of streptavidin. *J. Phys. Chem. B* 113, 8776 **(2009)**. © 2009. From [91], J. A. Howarter and J. P. Youngblood, Optimization of silica silanization by 3-aminopropyltriethoxysilane. *Langmuir* 22, 11142 **(2006)**. © 2006. From [102]. S. McFarlane, Biosensing using fluorescent-core microcapillaries, University of Alberta Masters Thesis **(2012)**. © (2012).

Biotin-avidin reactions are one of the most common test systems for new biosensor technologies, mainly because the binding chemistry is well understood and because of the exceptionally strong chemical affinity between biotin and streptavidin.[96–98] The functionalization can be based on the silane chemistry described above, since the $NH_2$ ends of the silane molecules bind to biotin through its carboxyl end. Alternatively, one can attach biotinylated BSA (bovine serum albumen) to the $–NH_2$ endgroups of the silane molecules. Using biotinylated BSA has the advantage that the expected wavelength shift is larger than it would be for the much smaller biotin molecule. BSA is a large protein that can have both carboxyl and amine end groups, and can thus bind to biotin and to the silanized capillary channel. Non-biotinylated BSA can also be used to block the silanized surface against nonspecific sticking of streptavidin or other proteins.[99] This can be a useful check that the surface chemistry is occurring as expected. A third option is to use silane functionalized polyethylene glycol (PEG) with the desired endgroup (e.g., silane-PEG-biotin).[100]

The last step is then the reaction of (strep)tavidin with the surface-bound biotin. The streptavidin protein is large compared to biotin; essentially the tetrahydrothiophene end of the biotin fits almost perfectly into the "divots" in the streptavidin, in one of the strongest non-covalent biomolecular binding reactions.[103] Successful tests have been performed both for microspheres,[104] which was one of the earliest demonstrations of capillary WGM based biosensing, and FCMs,[105] although in the latter case a significant amount of nonspecific streptavidin binding was reported. The reverse binding, in which streptavidin was attached to a surface that was first silanized and then activated for streptavidin using a bis (sulfosuccinimidyl) suberate solution, was used to show small molecule (biotin) detection in a highly sensitive LCORR.[106] Direct BSA binding to a silanized LCORR has also been established.[63]

Several other types of biomolecular sensing have been demonstrated, mainly also involving some form of silanization surface chemistry. For example, T4 bacteriophage virus was detected in an LCORR, at a level of $2.3 \times 10^3$ pfu/mL (plaque-forming units) using silanization followed by glutaraldehyde cross linking.[107] The R5C2 phage was also detected in an LCORR using the same surface functionalization method and detected

via streptavidin binding after blocking with BSA.[108] The 6-benzylaminopurine plant growth regulator was detected at a level of 0.01 mg/kg, using the same initial silanization + glutaraldehyde steps, followed by the application benzylaminopurine riboside antibody to the gluteraldehyde cross linker.[109] Phosphate-based pesticides were detected using similar methods, with the addition of AChE enzyme to the glutaraldehyde linker.[110] Detection limits were around $3.8 \times 10^{-11}$ M. HER2 breast-cancer-related antibodies were also reported at levels down to 13 ng/mL, by cross linking the LCORR surface with dimethyl pimelimidate dihydrochloride rather than glutaraldehyde.[111]

Almost all of these methods are based on initial silanization of the capillary channel. This is the key functionalization step; because of the potential difficulty with polymerization and the formation of less stable surfaces, it is imperative to run blanks (e.g., perform the same experiment without the silanization step or use a blocking agent) to ensure that the surface binding is indeed specific to the detected compound. The evidently wide range of possible biochemical sensor devices and the obvious success of many investigations over the past several years suggest that LCORRs and potentially FCMs can be versatile and very sensitive, and could even compete with surface-plasmon-based methods for many applications. The biggest difficulty, at the moment, is probably associated with the extreme mechanical fragility of thinned capillaries and the necessity to perform surface chemistry inside these fragile structures.



## 9. CONCLUSIONS AND OUTLOOK

The cylindrical whispering gallery modes of microcapillaries represent a highly sensitive and potentially promising means for microfluidic sensing and analysis. These devices are known alternatively as liquid core optical ring resonators, opto-fluidic ring resonators, or fluorescent core microcapillaries. In all cases, they utilize a thin high-refractive-index layer to confine radiation and develop the resonant modes of the structure. In LCORRs (which are essentially synonymous with opto-fluidic ring resonators, or "OFRRs"), the resonances form in the glass walls of a mechanically thinned capillary and are probed with a tunable laser system which is evanescently coupled to the device. In the FCM case, a high-index fluorescent layer is formed on the capillary channel and the resonances are probed with a spectrometer.

In this short review, the basic theory that permits the calculation of the mode field profile was first outlined. This is the first necessary step in the study of capillary (or fiber) WGM-based structures. LCORR and FCM structures were then compared and contrasted, showing the advantages and disadvantages of each sensor type. The LCORR is fundamentally a more sensitive device in almost all aspects, mainly because the resonances are better confined due to the large index contrast between the thinned capillary wall and the outside air (this contrast is much smaller in an FCM, where the outermost effective boundary is between the fluorescent layer and the thick-walled capillary). However, LCORRs have several troubling aspects including mechanical fragility and a rather difficult setup that requires careful positioning of optical elements. FCMs are far more robust, but they lack the amazing sensitivity of LCORR-type devices.

Next, we examined the various experimental setups that can be used for each structure. It can be quite difficult to determine the experimental difficulties from the short "experimental" section of most papers; hence two experimentally-oriented works were cited extensively. These efforts can be useful to prevent future investigators from spending a lot of time overcoming the same problems. Finally, a short summary of the recent applications of these devices was provided, with a few key aspects concerning the surface chemistry typically required to be performed in the capillary channel.

The future of this field remains open. A key aspect for LCORRs will concern the difficulty of integrating the fragile structure onto a workable device. In terms of sensor applications, FCMs lag behind LCORRs, partly because of their lower sensitivity but also, probably, because only a few groups have to date been able to make and test such structures. Alternative cylindrical WGM sensor structures not explicitly discussed in this brief review (e.g., lithographically patterned microdisks) are also very promising, with at least one company now selling diagnostic devices based on advanced microdisk technology.[112] The basic cylindrical resonances are mainly identical to those discussed here, but may include reflections from the top and bottom surfaces.

Future work will probably aim towards specific applications and packaging (i.e., how to integrate a complete detection system). Simple and more effective synthesis methods for FCMs are also desirable, and if the layer index can be increased, the sensitivity and detection limits of FCMs could approach LCORR values. Finally, the silica surface chemistry that occurs in the capillary channels is not always the same as for flat interfaces and has not been well-studied. The effects of pH can be critical and the exact values used in the capillary devices are rarely reported. Thus, the functionalization chemistry remains one of the most difficult and hard-to-reproduce steps in the development of targeted WGM-based capillary sensor devices.

**Acknowledgments:** Dr. Yanyan Zhi is thanked for an editorial review.

## References and Notes

1. B. H. Weigl and O. S. Wolfbeis, Capillary optical sensors. *Anal. Chem.* 66, 3323 **(1994)**.
2. O. S. Wolfbeis, Capillary waveguide sensors. *Trac. Trend Anal. Chem.* 15, 225 **(1996)**.

3. F. Baldini and A. Giannetti, Optical chemical and biochemical sensors: New trends. *Proc. SPIE* 5826, 485 **(2005)**.
4. P. V. Lambeck, Integrated optical sensors for the chemical domain. *Meas. Sci. Technol.* 17, R93 **(2006)**.
5. M. Borecki, M. L. Korwin-Pawlowski, M. Beblowska, J. Szmidt, and A. Jakubowski, Optoelectronic capillary sensors in microfluidic and point-of-care instrumentation, *Sensors* 10, 3771 **(2010)**.
6. J. Zhang, J. Hoogmartens, and A. Van Schepdael, Advances in capillary electrophoretically mediated microanalysis: An update. *Electrophoresis* 29, 56 **(2008)**.
7. E. Dabek-Zlotorzynska, V. Celo, and M. M. Yassine, Recent advances in CE and CEC of pollutants. *Electrophoresis* 29, 310 **(2008)**.
8. Z. El Rassi, Electrophoretic and electrochromatographic separation of proteins in capillaries: An update covering 2007–2009. *Electrophoresis* 31, 174 **(2010)**.
9. M. C. Breadmore, J. R. E. Thabano, M. Dawod, A. A. Kazarian, J. P. Quirino, and R. M. Guijt, Recent advances in enhancing the sensitivity of electrophoresis and electrochromatography in capillaries and microchips (2006–2008). *Electrophoresis* 30, 230 **(2009)**.
10. A. P. Lewis, A. Cranny, N. R. Harris, N. G. Green, J. A. Wharton, R. J. K. Wood, and K. R. Stokes, Review on the development of truly portable and *in-situ* capillary electrophoresis systems. *Meas. Sci. Technol.* 24, 042001 **(2013)**.
11. M. E. Bosch, A. J. Ruiz Sánchez, F. S. Rojas, and C. B. Ojeda, Recent development in optical fiber biosensors. *Sensors* 7, 797 **(2007)**.
12. S. Calixto, M. Rosete-Aguilar, D. Monzon-Hernandez, and V. P. Minkovich, Capillary refractometer integrated in a microfluidic configuration. *Appl. Opt.* 47, 843 **(2008)**.
13. L. E. Helseth, Simultaneous measurements of absorption spectrum and refractive index in a microfluidic system. *Opt. Express* 20, 4653 **(2012)**.
14. T. M. Squires and S. R. Quake, Microfluidics: Fluid physics at the nanoliter scale. *Reviews in Modern Physics* 77, 977 **(2005)**.
15. C. Yi, C.-W. Li, S. Ji, and M. Yang, Microfluidics technology for manipulation and analysis of biological cells. *Analytical Chimica Acta* 560, 1 **(2006)**.
16. B. Kuswandia, Nuriman, J. Huskens, and W. Verboom, Optical sensing systems for microfluidic devices: A review. *Analytical Chimica Acta* 601, 141 **(2007)**.
17. A. Chiasera, Y. Dumeige, P. Feron, M. Ferrari, Y. Jestin, G. N. Conti, S. Pelli, S. Soria, and G. C. Righini, Spherical whispering-gallery-mode microresonators, *Laser Photon. Rev.* 4, 457 **(2010)**.
18. F. Vollmer and S. Arnold, Whispering-gallery-mode biosensing: Label-free detection down to single molecules. *Nat. Methods* 5, 591 **(2008)**.
19. V. Lefévre-Seguin, Whispering-gallery mode lasers with doped silica microspheres. *Opt. Mater.* 11, 153 **(1999)**.
20. K. J. Vahala, Optical microcavities. *Nature* 424, 839 **(2003)**.
21. J.-M. Gérard and B. Gayral, Semiconductor microcavities, quantum boxes and the Purcell effect. *Lecture Notes in Physics* 531, 331 **(1999)**.
22. H. Yokoyama, Y. Nambu, and T. Kawakami, Controlling spontaneous emission and optical microcavities. *Confined Electrons and Photons, NATO ASI Series* 340, 427 **(1995)**.
23. M. V. Artemyev, U. Woggon, R. Wannemacher, H. Jaschinski, and W. Langbein, Light trapped in a photonic Dot: Microspheres act as a cavity for quantum dot emission. *Nano Lett.* 1, 309 **(2001)**.
24. S. Arnold, Spontaneous emission within a photonic atom: Radiative decay rates and spectroscopy of levitated microspheres. *Spectroscopy of Systems with Spatially Confined Structures NATO Science Series* 90, 465 **(2002)**.
25. K. Vahala, Optical microcavities. *Nature* 424, 839 **(2003)**.
26. A. Meldrum, P. Bianucci, and F. Marsiglio, Modification of ensemble emission rates and luminescence spectra for inhomogeneously broadened distributions of quantum dots coupled to optical microcavities. *Optics Express* 18, 10230 **(2010)**.
27. G. C. Righini, Y. Dumeige, P. Feron, M. Ferrari, G. N. Conti, D. Ristic, and S. Soria, Whispering gallery mode microresonators: Fundamentals and applications. *Rivista del Nuovo Cimento* 34, 435 **(2011)**.
28. J. B. Cole, N. Okada, and S. Banerjee, Advances in finite-difference time-domain calculation methods, Light Scattering Reviews, edited by A. A. Kokhanovsky, Springer-Verlag **(2012)**, pp. 115–179.
29. V. Zamora, A. Díez, M. V. Andrés, and B. Gimeno, Cylindrical optical microcavities: Basic properties and sensor applications. *Photonics and Nanostructures-Fundamentals and Applications* 9, 149 **(2011)**.
30. Lord Rayleigh, The problem of the whispering gallery, *Philos. Mag.* 20, 1001 **(1910)**.
31. C. V. Raman, On whispering galleries. *Proc. Indian Ass. Cult. Sci.* 7, 159 **(1921–1922)**.
32. G. Mie, Beitrage zur optik truber medien, *Ann. d. Physik* 25, 377 **(1908)**.
33. J. J. Thomson, Notes on Recent Research on Electricity and Magnetism Intended as a Sequel to Professor Clerk–Maxwell's Treatise on Electricity and Magnetism, Clarendon Press, Oxford **(1893)**.
34. A. Clebsch, Ueber die reflexion an einer Kugelfläche. *Journal für Mathematik*, 61, 195 **(1863)**.
35. L. Lorenz, Lysbevaegelsen i og uden for en af plane lysbolger belyst kugle. *Det Kongelige Danske Videnskabernes Selskabs Skrifter* 6, 1 **(1890)**.
36. L. Lorenz, Sur la lumière réfléchie et réfractée par une sphère (surface) transparente. In Oeuvres scientifiques de L. Lorenz. revues et annotées par H. Valentiner. Tome Premier, Libraire Lehmann & Stage, Copenhague **(1898)**, pp. 403–529.
37. P. Debye, Der Lichtdruck auf Kugeln von beliebigem Material. *Annalen der Physik*, Vierte Folge, Band 30. No. 1, 57 **(1909)**
38. H. Horvath, Gustav Mie and the scattering and absorption of light by particles: Historic developments and basics.*Journal of Quantitative Spectroscopy and Radiative Transfer* 110, 787 **(2009)**.
39. T. Wriedt, Mie Theory: A review. The Mie Theory, edited by W. Hergert and T. Wriedt, Springer Series in Optical Sciences, Springer-Verlag, Berlin Heidelberg **(2012)**, Vol. 169, DOI: 10.1007/978-3-642-28738-1_2.
40. A. N. Oraevsky, Whispering-gallery waves. *Quantum Electronics* 32, 377 **(2002)**.
41. A. B. Matsko and V. S. Ilchenko, Optical resonators with whispering-gallery modes—part I: Basics. *IEEE Journal of Selected Topics in Quantum Electronic* 12, 3 **(2006)**.
42. L. Prkna, J. Ctyroky, and M. Hubalek, Ring microresonator as a photonic structure with complex eigenfrequency. *Optical and Quantum Electronics* 36, 259 **(2004)**.
43. Y. V. Prokopenko, Y. F. Filippov, and I. A. Shipilova, Distribution of the field of whispering-gallery modes In a radially nonuniform two-layer cylindrical dielectric resonator. *Radiophysics and Quantum Electronics* 51, 561 **(2008)**.
44. C. F. Bohren and D. R. Huffman, Absorption and Scattering of Light by Small Particles, Wiley **(1998)**.
45. P. Bianucci, J. R. Rodriguez, F. Lenz, C. M. Clement, J. G. C. Veinot, and A. Meldrum, Silicon nanocrystal luminescence coupled to whispering gallery modes in optical fibers. *J. Appl. Phys.* 105, 023108 **(2009)**.
46. B. R. Johnson, Theory of morphology-dependent resonances: Shape resonances and width formulas. *Journal of the Optical Society of America A* 10, 343 **(1993)**.
47. S. Lane, J. Chan, T. Thiessen, and A. Meldrum, Whispering gallery mode structure and refractometric sensitivity of fluorescent capillary-type sensors. *Sensors and Actuators B: Chemical* 190, 752 **(2014)**.
48. J. A. Stratton, Electromagnetic Theory, McGraw-Hill, New York **(1941)**.

**49.** J. R. Buck and H. J. Kimble, Optimal sizes of dielectric microsphere for cavity QED with strong coupling. *Physical Review A* 67, 033806 **(2003)**.

**50.** R. Yang, A. Yun, Y. Zhang, and X. Pu, Quantum theory of whispering gallery modes in a cylindrical optical microcavity. *Optik* 122, 900 **(2011)**.

**51.** M. M. Popov, On the problem of whispering gallery waves in a neighborhood of a simple zero of the effective curvature of the boundary. *Journal of Soviet Mathematics* 11, 791 **(1979)**.

**52.** I. M. White, H. Oveys, and X. Fan, Liquid–core optical ring-resonator sensors. *Opt. Lett.* 31, 1319 **(2006)**.

**53.** P. Bianucci, Y. Y. Zhi, F. Marsiglio, J. Silverstone, and A. Meldrum, Microcavity effects in ensembles of silicon quantum dots coupled to high-Q resonators. *Physica Status Solidi A* 208, 639 **(2011)**.

**54.** T. Ling and L. J. Guo, Analysis of the sensing properties of silica microtube resonators, *Journal of the Optical Society of America B*, 26, 471 **(2009)**.

**55.** R. D. Kekatpure and M. L. Brongersma, Fundamental photophysics and optical loss processes in Si-nanocrystal-doped microdisk resonators. *Physical Review A* 78, 023829 **(2008)**.

**56.** L. H. Agha, J. E. Sharping, M. A. Foster, and A. L. Gaeta, Optimal sizes of silica microspheres for linear and nonlinear optical interactions. *Applied Physics B* 83, 303 **(2006)**.

**57.** J. W. Silverstone, S. McFarlane, C. P. K. Manchee, and A. Meldrum, Ultimate resolution for refractometric sensing with whispering gallery mode microcavities. *Opt. Express* 20, 8284 **(2012)**.

**58.** K. J. Rowland, A. Francois, P. Hoffmann, and T. M. Monro, Fluorescent polymer coated capillaries as optofluidic refractometric sensors. *Opt. Express* 21, 11492 **(2013)**.

**59.** I. Teraoka, S. Arnold, and F. Vollmer, Perturbation approach to resonance shifts of whispering-gallery modes in a dielectric microsphere as a probe of a surrounding medium. *Journal of the Optical Society of America B* 20, 1937 **(2003)**.

**60.** I. Teraoka and S. Arnold, Enhancing sensitivity of a whispering gallery mode microsphere sensor by a high-refractive index surface layer. *Journal of the Optical Society of America B* 23, 1434 **(2006)**.

**61.** I. Teraoka, S. Arnold, and F. Vollmer, Whispering-gallery modes in a microsphere coated with a high-refractive index layer: Polarization-dependent sensitivity enhancement of the resonance-shift sensor and TE-TM resonance matching. *Journal of the Optical Society of America B* 24, 657 **(2007)**.

**62.** S. Lane, F. Marsiglio, Y. Zhi, and A. Meldrum, *Appl. Opt.* (in review).

**63.** H. Zhu, I. M. White, J. D. Suter, P. S. Dale, and X. Fan, Analysis of biomolecule detection with optofluidic ring resonator sensors. *Opt. Express* 15, 9139 **(2007)**.

**64.** C.-Y. Chao and L. J. Guo, Design and optimization of microring resonators in biochemical sensing applications. *Journal of Lightwave Technology* 24, 1395 **(2006)**.

**65.** C.-Y. Chao, W. Fung, and L. J. Guo, Polymer microring resonators for biochemical sensing applications. *IEEE Journal of Selected Topics in Quantum Electronics* 12, 134 **(2006)**.

**66.** C.-Y. Chao and L. J. Guo, Design and optimization of microring resonators in biochemical sensing applications. *Journal of Lightwave Technology* 24, 1395 **(2006)**.

**67.** C.-Y. Chao, W. Fung, and L. J. Guo, Polymer microring resonators for biochemical sensing applications. *IEEE Journal of Selected Topics in Quantum Electronics* 12, 134 **(2006)**.

**68.** I. M. White and X. Fan, On the performance quantification of resonant refractive index sensors. *Opt. Express* 16, 1020 **(2008)**.

**69.** I. M. White, H. Zhu, J. D. Suter, X. Fan, and M. Zourob, Label-free detection with the liquid core optical ring resonator sensing platform, Methods in Molecular Biology: Biosensors and Biodetection, edited by A. Rasooly and K. E. Herold, Humana Press, a part of Springer Science + Business Media, LLC **(2009)**, Vol. 503.

**70.** S. McFarlane, C. P. K. Manchee, J. W. Silverstone, J. G. C. Veinot, and A. Meldrum, Synthesis and operation of fluorescent-core microcavities for refractometric sensing. *Journal of Visualized Experiments* 73, e50256 **(2013)**.

**71.** C. P. K. Manchee, V. Zamora, J. Silverstone, J. G. C. Veinot, and A. Meldrum, Refractometric sensing with fluorescent-core microcavities. *Opt. Express* 19, 21540 **(2011)**.

**72.** G. Huang, Q. Bolanos, V. A. Bolanos, F. Ding, S. Kiravittaya, Y. Mei, and O. G. Schmidt, Rolled-up optical microcavities with subwavelength wall thicknesses for enhanced liquid sensing applications. *ACS Nano* 4, 3123 **(2010)**.

**73.** P. Measor, L. Seballos, D. Yin, J. Z. Zhang, E. J. Lunt, A. R. Hawkins, and H. Schmidt, On-chip surface-enhanced Raman scattering detection using integrated liquid–core waveguides. *Appl. Phys. Lett* 90, 211107 **(2007)**.

**74.** J. D. Suter, I. M. White, H. Zhu, and X. Fan, Thermal characterization of liquid core optical ring resonator sensors. *Appl. Opt.* 46, 389 **(2007)**.

**75.** N. Lin, L. Jiang, S. Wang, H. Xiao, Y. Lu, and H.-L. Tsai, Design and optimization of liquid core optical ring resonator for refractive index sensing. *Appl. Opt.* 50, 3615 **(2011)**.

**76.** L. Ding, P. Senellart, A. Lemaitre, S. Ducci, G. Leo, and I. Favero, GaAs micro-nanodisks probed by a looped fiber taper for optomechanics applications, Nanophotonics III, edited by D. L. Andrews, J.-M. Nunzi, and A. Ostendorf, *Proc. of SPIE* **(2010)**, Vol. 7712, pp. 771211.

**77.** C. Baker, C. Belacel, A. Andronico, P. Senellart, A. Lemaitre, E. Galopin, S. Ducci, G. Leo, and I. Favero, Critical optical coupling between a GaAs disk and a nanowaveguide suspended on the chip. *Appl. Phys. Lett.* 99, 151117 **(2011)**.

**78.** S. M. Spillane, T. J. Kippenberg, O. J. Painter, and K. J. Vahala, Ideality in a fiber-taper-coupled microresonator system for application to cavity quantum electrodynamics. *Phys. Rev. Lett.* 91, 043902 **(2003)**.

**79.** A. Morand, Y. Zhang, B. Martin, K. P. Huy, D. Amans, and P. Benech, Ultra-compact microdisk resonator filters on SOI substrate. *Opt. Express* 25, 12814 **(2006)**.

**80.** E. F. Franchimon, K. R. Hiremath, R. Stoffer, and M. Hammer, *Journal of the Optical Society of America B* 30, 1048 **(2013)**.

**81.** J. A. Lock, Morphology-dependent resonances of an infinitely long circular cylinder illuminated by a diagonally incident plane wave or a focused Gaussian beam. *Journal of the Optical Society of America A* 14, 653 **(1997)**.

**82.** A. W. Poon, R. K. Chang, and J. A. Lock, Spiral morphology-dependent resonances in an optical fiber: Effects of fiber tilt and focused Gaussian beam illumination. *Opt. Lett.* 23, 1105 **(1998)**.

**83.** V. Zamora, A. Díez, M. V. Andrés, and B. Gimeno, Refractometric sensor based on whispering-gallery modes of thin capillaries. *Opt. Express* 15, 12011 **(2007)**.

**84.** V. Zamora, A. Díez, M. V. Andrés, and B. Gimeno, Interrogation of whispering-gallery modes resonances in cylindrical microcavities by backreflection detection. *Opt. Lett.* 34, 1039 **(2009)**.

**85.** A. L. Stancik and E. B. Brauns, A simple asymmetric lineshape for fitting infrared absorption spectra. *Vibr. Spectr.* 47, 66 **(2008)**.

**86.** V. Zamora, Z. Zhang, and A. Meldrum, Refractometric sensing of heavy oils in fluorescent core microcapillaries. *Oil and Gas Science and Technology—Rev. IFP Energies Nouvelles* 2013113 **(2013)**.

**87.** N. Aissaoui, L. Bergaoui, J. Landoulsi, J.-F. Lambert, and S. Boujday, Silane Layers on Silicon Surfaces: Mechanism of interaction, stability, and influence on protein adsorption. *Langmuir* 28, 656 **(2012)**.

**88.** D. Knopp, D. Tang, and R. Niessner, Review: bioanalytical applications of biomolecule-functionalized nanometer-sized doped silica particles. *Anal. Chim. Acta* 647, 14 **(2009)**.

**89.** J. J. Cras, C. A. Rowe-Taitt, D. A. Nivens, and F. S. Ligler, Comparison of chemical cleaning methods of glass in preparation for silanization. *Biosens. Bioelectron.* 14, 683 **(1999)**.

**90.** A. V. Krasnoslobodtsev and S. N. Smirnov, Effect of water on silanization of silica by trimethoxysilanes. *Langmuir* 18, 3181 **(2002)**.

**91.** J. A. Howarter and J. P. Youngblood, Optimization of silica silanization by 3-Aminopropyltriethoxysilane. *Langmuir* 22, 11142 **(2006)**.

**92.** I. M. White, S. I. Shapova, H. Zhu, J. D. Suter, S. Lacey, P. Zhang, H. Oveys, L. Brewington, J. Gohring, and X. Fan, Applications of the liquid core optical ring resonator platform, *Proc. of SPIE* 6757, 675707 **(2007)**.

**93.** J. D. Suter, I. M. White, H. Zhu, H. Shi, C. W. Caldwell, and X. Fan, Label-free quantitative DNA detection using the liquid core optical ring resonator. *Biosens. Bioelectron.* 23, 1003 **(2008)**.

**94.** A. Carré, V. Lacarrière, and W. Birch, Molecular interactions between DNA and an aminated glass substrate. *J. Colloid Interface Sci.* 260, 49 **(2003)**.

**95.** J. D. Sutera, D. J. Howard, H. Shi, C. W. Caldwell, and X. Fan, Label-free DNA methylation analysis using opto-fluidic ring resonators, *Biosens. Bioelectron.* 26, 1016 **(2010)**.

**96.** E. P. Diamandis and T. K. Christopoulos, The biotin-(strept)avidin system: Principles and applications in biotechnology. *Clin. Chem.* 37, 625 **(1991)**.

**97.** See for example Avidin-Biotin Interactions: Methods in Molecular Biology, edited by R. J. McMahon, Springer, Humana Press **(2008)**.

**98.** J. Wong, A. Chilkoti, and V. T. Moy, Direct force measurements of the streptavidin–biotin interaction. *Biomol. Eng* 16, 45 **(1999)**.

**99.** Y. L. Jeyachandran, J. A. Mielczarski, E. Mielczarski, and B. Rai, Efficiency of blocking of non-specific interaction of different proteins by BSA adsorbed on hydrophobic and hydrophilic surfaces. *J. Colloid Interface Sci.* 341, 136 **(2010)**.

**100.** A. S. Anderson, A. M. Dattelbaum, G. A. Montaño, D. N. Price, J. G. Schmidt, J. S. Martinez, W. K. Grace, K. M. Grace, and B. I. Swanson, Functional PEG-modified thin films for biological detection. *Langmuir* 2008, 2240 **(2008)**.

**101.** N. A. Lapin and Y. J. Chabal, Infrared characterization of biotinylated silicon oxide surfaces, surface stability, and specific attachment of streptavidin. *J. Phys. Chem. B*, 113, 8776 **(2009)**.

**102.** S. McFarlane, Biosensing using fluorescent-core microcapillaries, University of Alberta Masters Thesis **(2012)**.

**103.** P. S. Stayton, S. Freitag, L. A. Klumb, A. Chilkoti, V. Chu, J. E. Penzotti, R. To, D. Hyre, I. Le Trong, T. P. Lybrand, and R. E. Stenkamp, Streptavidin-biotin binding energetics. *Biomol. Eng.* 16, 39 **(1999)**.

**104.** F. Vollmer, D. Braun, A. Libchaber, M. Khoshsima, I. Teraoka, and S. Arnold, Protein detection by optical shift of a resonant microcavity. *Appl. Phys. Lett.* 21, 4507 **(2002)**.

**105.** S. McFarlane, C. P. K. Manchee, J. W. Silverstone, J. G. C. Veinot, and A. Meldrum, Feasibility of a fluorescent-core microcapillary for biosensing applications. *Sensor Lett.* 11, 1513 **(2013)**.

**106.** H. Li and X. Fan, Characterization of sensing capability of optofluidic ring resonator biosensors. *Appl. Phys. Lett.* 97, 011105 **(2010)**.

**107.** H. Zhu, I. M. White, J. D. Suter, M. Zourob, and X. Fan, Opto-fluidic micro-ring resonator for sensitive label-free viral detection. *Analyst* 133, 356 **(2008)**.

**108.** H. Zhu, I. M. White, J. D. Suter, and X. Fan, Phage-based label-free biomolecule detection in an opto-fluidic ring resonator. *Biosens. Bioelectron.* 24, 461 **(2008)**.

**109.** A. Lee, G.-Y. Kim, and J.-H. Moon, Detection of 6-benzylaminopurine plant growth regulator in bean sprouts using OFRR biosensor and QuEChERS method. *Analytical Methods* 5, 961 **(2013)**.

**110.** Gilmo Yang a, b, Ian M. White a, and Xudong Fan, An opto-fluidic ring resonator biosensor for the detection of organophosphorus pesticides. *Sens. Actuators, B* 133, 105 **(2008)**.

**111.** J. T. Gohring, P. S. Dale, and X. Fan, Detection of HER2 breast cancer biomarker using the opto-fluidic ring resonator biosensor. *Sens. Actuators, B* 146, 226 **(2010)**.

**112.** See http://genalyte.com/.